
MiniMaxAD: A Lightweight Autoencoder for Feature-Rich Anomaly Detection

Fengjie Wang Chengming Liu Lei Shi Pang Haibo*
Zhengzhou University, China
oo.ggg42@gmail.com
{cmliu, shilei, phb}@zzu.edu.cn

Abstract

Previous unsupervised anomaly detection (UAD) methods often struggle with significant intra-class diversity; i.e., a class in a dataset contains multiple subclasses, which we categorize as Feature-Rich Anomaly Detection Datasets (FRADs). This challenge is evident in applications such as unified setting and unmanned supermarket scenarios. To address this challenge, we developed MiniMaxAD, a lightweight autoencoder designed to efficiently compress and memorize extensive information from normal images. Our model employs a technique that enhances feature diversity, thereby increasing the effective capacity limit of the network. It also utilizes large kernel convolution to extract highly abstract patterns, which contribute to efficient and compact feature embedding. Moreover, we introduce an Adaptive Contraction Loss (ADCLoss), specifically tailored to FRADs, to address the limitations of the global cosine distance loss. In our methodology, any dataset can be unified under the framework of feature-rich anomaly detection, in a way that the benefits far outweigh the drawbacks. MiniMaxAD underwent comprehensive testing across six challenging UAD benchmarks, achieving state-of-the-art results in four and highly competitive outcomes in the remaining two. Notably, our model not only achieved state-of-the-art performance in unmanned supermarket tasks but also exhibited an inference speed 37 times faster than the previous best method, demonstrating its effectiveness in complex UAD tasks.

1 Introduction

Anomaly detection presents a significant challenge in the field of computer vision. Owing to the difficulties associated with collecting and labeling anomalous samples, unsupervised learning methods have become increasingly favored for anomaly detection. These methods utilize only normal samples for training and are engineered to identify anomalous images and segment anomalous regions during inference. Recent advancements in unsupervised anomaly detection (UAD) methods [1; 2; 3; 4; 5; 6] have shown impressive performance on several widely acknowledged industrial anomaly detection datasets [7; 8; 9]. In addition, UAD technology is increasingly used in more complex scenarios to meet growing demand.

Existing anomaly detection methods often require training a separate model for each class of objects, which can lead to significant memory consumption. In response, UniAD [10] proposes a unified setting that trains a single model on multiple classes of normal samples. They also highlight the limitations of the traditional one-category-one-model approach, especially in cases where normal samples exhibit considerable intra-class diversity. This challenge is particularly evident in the unmanned supermarket sector, as demonstrated by the newly introduced GoodsAD [11] dataset, which features significant intra-class diversity with a single product offered by multiple brands.

*Corresponding Author

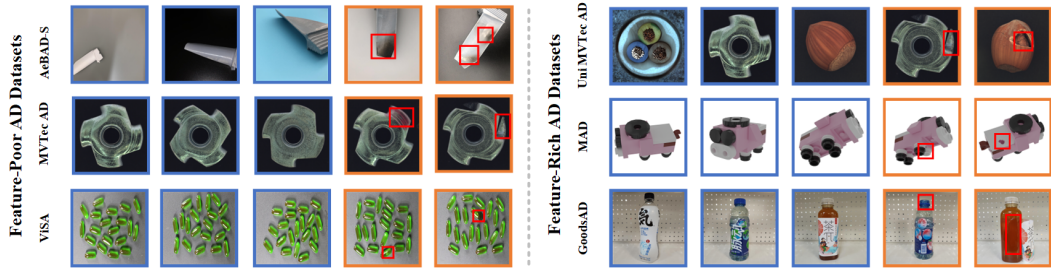


Figure 1: Comparison of Feature-Rich Anomaly Detection Datasets (FRADs) and Feature-Poor Anomaly Detection Datasets (FPADs). Anomalous areas are marked with red boxes.

Notably, methods that previously performed well often struggle on this task, underscoring the need for more adaptable methods.

In this work, we revisit existing UAD datasets, categorizing them based on the level of intra-class feature diversity. We define datasets with substantial intra-class diversity as Feature-Rich Anomaly Detection Datasets (FRADs), in contrast to Feature-Poor Anomaly Detection Datasets (FPADs), as illustrated in Figure 1. Notably, FPADs can be easily converted to FRADs using the unified setting. The unified setting and the Multi-Pose Dataset (MAD) [12] are classified as FRADs due to their pronounced intra-class diversity: the former is an extreme case, while the latter, which comprises images of the same object in different poses, also exhibits significant diversity within the same category. This diversity necessitates that neural networks extensively memorize normal features. Among FRADs, PatchCore [13] demonstrates superior performance in applications such as unmanned supermarkets [11] and multi-view scenarios [12], benefiting from an efficient memory bank that stores normal contexts. However, this approach also significantly increases inference times due to its reliance on time-consuming query operations. Additionally, as the number of training samples grows, so does the memory bank’s size, complicating the application of PatchCore in unified settings. Consequently, we aim to develop a high-performance, lightweight UAD method that addresses the challenges of FRADs effectively.

Methods based on multi-scale reconstruction [14; 5; 2; 15; 16; 17] are celebrated for their simplicity and efficiency. These methods use a paired encoder and decoder to reconstruct features, effectively capturing the manifold of normal samples. During testing, areas with higher reconstruction errors are flagged as anomalies. However, they face two primary challenges: (a) the network’s limited information capacity may inadequately reconstruct normal areas, resulting in false positives; (b) its robust generalization ability might allow it to accurately reconstruct abnormal areas, leading to false negatives, a phenomenon often referred to as the "identical shortcut" [10]. Experimental results from GoodsAD [11] and PAD [12] show that these methods tend to generate a high rate of false positives by mistakenly classifying many normal foreground regions as abnormal in FRADs. Moreover, replacing the backbone of Reverse Distillation (RD) [14] with a larger model, such as WideResNet-101 [18], significantly reduces performance, as illustrated in Figure 3(a). This suggests that dual challenges of limited capacity and the "identical shortcut" are present when dealing with FRADs.

In response to the dual challenges, our study introduces a core motivation: **maximizing the "effective capacity" of a lightweight autoencoder**. Inspired by ConvNeXtV2 [19], which introduced Global Response Normalization (GRN) to counteract "feature collapse", a phenomenon where numerous feature maps become inactive or redundant across channels, we have incorporated the GRN Unit to enhance feature diversity and thereby increase the upper limit of network capacity. Additionally, we employ large kernel convolution to extract more profound abstract patterns. As a result, we utilized UniRepLKNet-N [20], a large kernel convolutional network equipped with a GRN unit, compatible with the RD framework. Furthermore, we propose a novel quantile-based adaptive contraction loss (ADCLoss), addressing the challenges of optimizing global cosine distance loss on FRADs and significantly improving performance while preventing overfitting. To adapt to the distinct characterization of FRADs and FPADs, we present two variants of our model: **MiniMaxAD-fr** and **MiniMaxAD-fp**, each utilizing different loss functions tailored to their respective datasets. Extensive experiments were conducted across two FPADs—industrial images VisA [8] and aero-engine images AeBAD-S [15], and four FRADs including MVTEC AD [7], VisA [8] under the unified

setting, unmanned supermarket images GoodsAD [11], and multi-pose images MAD [12]. The results demonstrate that our method not only operates efficiently but also achieves state-of-the-art results, particularly in image-level anomaly detection on GoodsAD, surpassing the previous best method, PatchCore-100% [13], with a Frames Per Second (FPS) rate 37 times greater. Intriguingly, MiniMaxAD-fr achieves an impressive 96.9% I-AUROC in the unified setting of ViSA, surpassing MiniMaxAD-fp under a one-category-one-model setting by 0.5%. This achievement demonstrates that MiniMaxAD-fr efficiently embeds the context of 12 image categories, totaling 8,659 normal images, into just 89MB of storage. Our main contributions are summarized below.

- We revisited existing UAD datasets, classifying them into Feature-Rich Anomaly Detection Datasets (FRADs) and Feature-Poor Anomaly Detection Datasets (FPADs), justified by a comprehensive ablation study. We also provide a unified solution for both types of datasets.
- We introduced a new design paradigm for anomaly detection methods based on multi-scale reconstruction, aimed at maximizing the "effective capacity" of a lightweight autoencoder, which reduces memory costs and significantly improves performance.
- We developed a novel Adaptive Contraction Loss (ADCLoss) tailored for FRADs, effectively addressing the optimization challenges associated with feature-rich datasets using global cosine distance loss.
- Our comprehensive experiments show that our method achieves state-of-the-art performance across multiple challenging tasks.

2 Method

Our study is based on the Reverse Distillation (RD) framework, which is broadly a multi-scale autoencoder. We will first summarize the classic RD methods, and use our core motivation to guide our detailed explanation of the complete MiniMaxAD methodology.

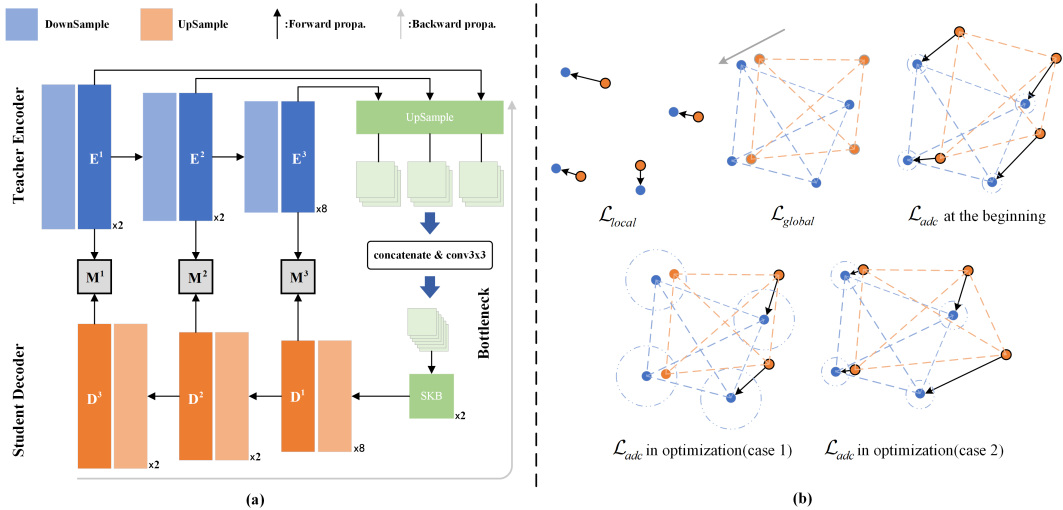


Figure 2: **(a) Overview of Proposed MiniMaxAD:** MiniMaxAD’s architecture deviates from the RD approach by incorporating a Decoder that is fully symmetrical to the Encoder, including an identical number of blocks stacked in each layer. The bottleneck layer employs a 3x3 downsampled convolution along with two SmaK Blocks. **(b) Optimization Process of the Loss Function:** The diagram illustrates the optimization direction using arrows. Within the blue dashed circle, the yellow circle will not be optimized, i.e., the gradient will be stopped. As overall alignment improves, the radius of the blue dashed circle increases. During the optimization of \mathcal{L}_{adc} , moving a single yellow circle outward in the lower right corner of Case 1 causes the blue dashed circle to contract, leading to Case 2. This adjustment encourages additional yellow circles to enter the optimization process.

2.1 Reverse Distillation for Anomaly Detection

Reverse Distillation (RD) [14] is an important method in UAD, featuring a streamlined architecture that consists of a frozen pre-training encoder (teacher), a bottleneck, and a feature reconstruction decoder (student). The encoder extracts multi-scale spatial features from the input image, which the bottleneck then condenses to minimize redundancy. The decoder, designed as an inverse but not a perfectly symmetrical counterpart to the encoder, reconstructs the encoder’s output to achieve feature-level alignment. When faced with abnormal samples during testing, the decoder’s inability to accurately reconstruct the encoder’s output serves to highlight discrepancies, thereby generating an anomaly map. Formally, let $f_E^k, f_D^k \in \mathbb{R}^{C_k \times H_k \times W_k}$ represent the feature maps output by the encoder and decoder at the k -th level, respectively. Here, C_k , H_k , and W_k denote the number of channels, the height, and the width of the output feature map at each level. The training objective is to minimize the local cosine distance loss between the corresponding output features of each layer for normal images, quantified by the following formula:

$$\mathcal{L}_{local} = \sum_{k=1}^3 \frac{1}{H^k W^k} \sum_{h=1}^{H^k} \sum_{w=1}^{W^k} \left(1 - \frac{f_E^k(h, w)^T \cdot f_D^k(h, w)}{\|f_E^k(h, w)\| \|f_D^k(h, w)\|} \right) \quad (1)$$

Where $\|\cdot\|$ denotes the L2-norm, and a set (h, w) specifies a spatial point on the feature map. ReContrast [5] identified a likely coding error in the official implementation of RD, wherein an additional flattening operation was performed during the cosine distance calculation. To address this issue, they proposed a modification to the optimization objective in the RD framework by introducing a global cosine distance loss, described as follows:

$$\mathcal{L}_{global} = \sum_{k=1}^3 \left(1 - \frac{\mathcal{F}(f_E^k)^T \cdot \mathcal{F}(f_D^k)}{\|\mathcal{F}(f_E^k)\| \|\mathcal{F}(f_D^k)\|} \right) \quad (2)$$

Where \mathcal{F} represents the flattening operation. For the feature tensors f_E^k and f_D^k , point-by-point differences are calculated using the local cosine distance. This process generates a two-dimensional anomaly map, denoted by $m^k \in \mathbb{R}^{H_k \times W_k}$.

$$m^k(h, w) = 1 - \frac{f_E^k(h, w)^T \cdot f_D^k(h, w)}{\|f_E^k(h, w)\| \|f_D^k(h, w)\|} \quad (3)$$

Ultimately, m^k is upsampled to match the height and width of the original image, $I \in \mathbb{R}^{C_0 \times H_0 \times W_0}$, using an operation represented by Ψ . The final anomaly score map, $\mathcal{S}(h, w) \in \mathbb{R}^{H_0 \times W_0}$, is then constructed by aggregating pixel values across three layers of sub-anomaly maps:

$$\mathcal{S}(h, w) = \sum_{k=0}^3 \Psi(m^k) \quad (4)$$

2.2 GRN Unit for Expanding the Effective Capacity Cap

Inspired by recent advances in visual recognition, we have incorporated a Global Response Normalization (GRN) unit [19] to enhance feature diversity and, consequently, the upper limit of the effective network capacity. Specifically, the GRN unit boosts channel contrast and selectivity by aggregating features at the channel level. This is achieved using the L2-norm on the feature map X_i , followed by normalization to compute the feature normalization coefficient n_x :

$$n_x = \frac{g_x}{\mathbf{E}[g_x]} \in \mathcal{R}^C \quad (5)$$

where $g_x = \{\|X_1\|, \|X_2\|, \dots, \|X_C\|\} \in \mathcal{R}^C$, and $\mathbf{E}[\cdot]$ represents the computation of the mean. This equation determines the relative importance of each channel, fostering a competitive relationship among them through mutual suppression. The computed feature normalization coefficients n_x are then used to calibrate the raw input:

$$X = \gamma * (X * n_x) + \beta + X \quad (6)$$

where γ and β are learnable hyperparameters. The GRN unit enhances feature diversity, making it particularly effective within the multi-scale reconstruction framework for addressing capacity limitations. We will illustrate the intuitive effects of the GRN unit in the next subsection.

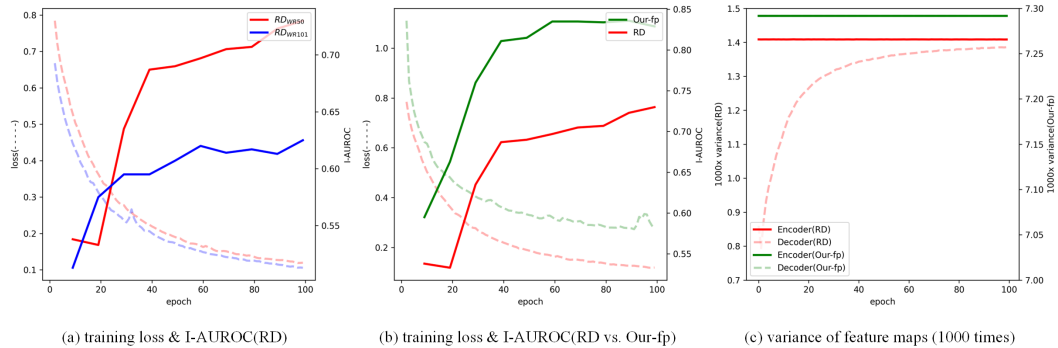


Figure 3: **(a)** Performance comparison of RD with different backbones for the drink can scenario in the GoodsAD dataset. **(b)** Performance comparison between RD and MiniMaxAD for the *drink can* scenario. **(c)** Feature alignment process of RD and MiniMaxAD when trained on *drink can*, viewed from the perspective of feature diversity, shows that the two green lines overlap.

2.3 Towards Maximize Effective Information Capacity

Our core motivation can be articulated in two ways: (1) to limit the "identical shortcut" phenomenon by employing a relatively lightweight autoencoder, and (2) to maximize the "**effective capacity**" of the autoencoder, where "**effective**" emphasizes the model's ability to reconstruct normal foreground regions and "**capacity**" emphasizes greater information density. Based on this premise, an intuitive strategy is to extract deeper, more abstract representations to achieve highly compact information storage. Consequently, large kernel convolution emerges as a powerful method for implementing this strategy. In recent visual recognition research, advances in large kernel convolution have renewed interest in convolutional networks. UniRepLKNet [20] proposes a series of design guidelines for large-kernel convolutions; they have developed a powerful backbone equipped with a GRN Unit that perfectly fits our methodology. This network comprises several downsampling blocks and two distinct types of blocks—the Large Kernel Block (LarK Block) and the Small Kernel Block (SmaK Block). As shown in the encoder section of the Figure 2(a). Specifically, E^1 utilizes the SmaK Block, while E^2 and E^3 deploy the LarK Block.

The residual connectivity within these blocks enhances spatial aggregation and inter-channel communication, increasing the network's depth. The SmaK Block's residual connectivity mirrors that of the ConvNeXt, incorporating a depthwise (DW) convolution layer and a FeedForward Network (FFN) with a GRN unit. Unlike ConvNeXt, however, it replaces LayerNorm with BatchNorm and adds an SE Block after the DW layer to facilitate global average pooling and nonlinear mapping of the pooled vectors. These modifications improve spatial aggregation transformation and channel mixing. The primary distinction between the LarK and SmaK Blocks lies in the former's use of a Dilated Reparam layer instead of the latter's DW 3×3 convolution layer. This layer combines a large kernel convolution with parallel small kernel convolutions, proving advantageous for capturing small-scale patterns during training. During inference, the structural reparameterization method [21] fuses multiple convolutional kernels into a single large kernel, thus enhancing representation power and accelerating inference. The full architecture of the proposed model is depicted in Figure 2(a).

To illustrate the substantial advantages of MiniMaxAD over RD in handling FRADs, we conducted a quantitative analysis of the feature map alignment process, where the Decoder reconstructs the Encoder's features. We perform the L2-norm on the feature maps of the encoder and decoder, after which the variance was calculated as $\frac{1}{3} \sum_{k=1}^3 \sigma(f_E^k / \|f_E^k\|)^2$ and $\frac{1}{3} \sum_{k=1}^3 \sigma(f_D^k / \|f_D^k\|)^2$. As depicted in Figure 3(c), benefiting from the GRN units, the variance of MiniMaxAD is about five times that of RD, indicating that MiniMaxAD can characterize richer information. We conduct a more analysis of this process from the perspective of entropy, detailed in the Appendix D. Additionally, Figure 3(b) shows that while RD's global cosine distance loss is lower than MiniMaxAD's, RD's Image-level AUROC is significantly worse. This suggests that the reduced feature diversity in WideResNet-50 simplifies the decoder's alignment task, whereas MiniMaxAD's greater feature diversity better supports complex anomaly detection.

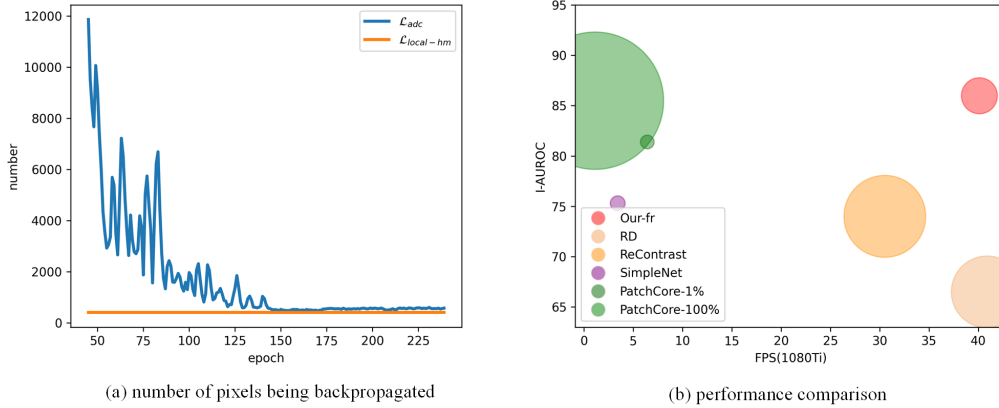


Figure 4: **(a)** The fixed mining strategy consistently results in a low number of pixels for backpropagation. In contrast, the Adaptive Contraction Strategy optimizes across a range from full-image coverage to extremely small localities. **(b)** Anomaly Detection Performance vs. FPS and Model Storage Size (excluding pre-training network occupancy): Each I-AUROC value averages image-level detection AUROC from the GoodsAD dataset.

2.4 Adaptive Contraction Strategies Tailored to Optimize FRADs

ReContrast [5] introduced a hard mining strategy based on \mathcal{L}_{global} , which selectively discards gradients from the background region and concentrates on optimizing the foreground regions. This approach aims to increase the discrepancy between the reconstruction errors due to anomalies and those observed in all normal regions. Ideally, reducing \mathcal{L}_{global} to zero would be akin to minimizing \mathcal{L}_{local} to zero. However, in practice, the absence of direct guidance from \mathcal{L}_{local} complicates the model’s convergence to the global optimum, especially in FRADs. Intuitively, foreground regions should exhibit spatial consistency across the three levels of sub-anomaly maps. Consequently, we directly optimize the final anomaly map, $\mathcal{S}(h, w) \in \mathbb{R}^{H_0 \times W_0}$, by modifying \mathcal{L}_{local} to:

$$\mathcal{L}_{local} = \frac{1}{HW} \sum_{h=1}^H \sum_{w=1}^W \mathcal{S}(h, w)^2 \quad (7)$$

Our newly introduced \mathcal{L}_{local} is conceptually similar to applying an MSE loss between the zero tensor and the final anomaly map, $\mathcal{S}(h, w)$. Inspired by the hard feature loss proposed by EfficientAD [6], we have devised a dynamic contraction strategy for \mathcal{L}_{local} , specifically designed to accommodate the distinctive numerical characteristics of the anomaly map. We define p_{hard} as the primary mining factor and p_{lim} as the lower bound mining factor. Consider α to be the p_{hard} -quantile of the elements in $\mathcal{S}(h, w)$, and β to be the p_{lim} -quantile of the squared elements, $\mathcal{S}(h, w)^2$. Additionally, let σ represent the standard deviation of $\mathcal{S}(h, w)$. The number of pixels satisfying $\mathcal{S}(h, w)^2 \geq \alpha - \sigma^2$ is denoted by \mathcal{A} . The number of pixels influenced by the lower bound mining factor p_{lim} is indicated by \mathcal{B} , calculated as $B \times H_0 \times W_0 \times (1 - p_{lim})$, where B is the batch size. We also define a mean operation, $\mathbf{E}(\mathcal{S}|\mathcal{C})$, where elements that do not satisfy the condition \mathcal{C} will stop the gradient and not participate in the mean computation. Our proposed ADCLoss is structured as follows:

$$\mathcal{L}_{adc} = \begin{cases} \mathbf{E}(\mathcal{S}^2 \mid \mathcal{S}^2 \geq \alpha - \sigma^2), & \text{if } \mathcal{A} \geq \mathcal{B} \\ \mathbf{E}(\mathcal{S}^2 \mid \mathcal{S}^2 \geq \beta - \sigma^2), & \text{if } \mathcal{A} < \mathcal{B} \end{cases} \quad (8)$$

This adaptive contraction strategy ensures that the property of global sensing is maintained throughout the entire optimization process of \mathcal{L}_{adc} . This adaptive contraction process is illustrated in Figure 4(a). By default, p_{hard} is set to 0.9999 and p_{lim} to 0.9995. The optimization process of \mathcal{L}_{adc} is depicted in Figure 2(b). We characterize the loss function of a fixed mining strategy as:

$$\mathcal{L}_{local-hm} = \mathbf{E}(\mathcal{S}^2 \mid \mathcal{S}^2 \geq \beta) \quad (9)$$

Ultimately, we provide two variants of our model: MiniMaxAD-fr and MiniMaxAD-fp. MiniMaxAD-fr is equipped with \mathcal{L}_{adc} specifically for processing FRADs, while MiniMaxAD-fp uses \mathcal{L}_{global} to handle FPADs.

Table 1: Anomaly detection and segmentation results with AUPRO/I-AUROC(%) on AeBAD-S.

	DRAEM[1]	PatchCore[13]	RD[2]	MMR[15]	Our-fp
Same	71.4/64.0	89.5/75.2	86.4/82.4	89.6/85.6	78.7/ 86.4
Background	44.3/62.1	89.4/74.1	86.4/84.3	90.1/84.4	80.0/ 90.7
Illumination	67.6/61.6	88.2/74.6	86.7/84.3	90.2/88.8	84.1/87.2
View	71.1/62.3	84.0/60.1	82.9/71.9	86.3/79.9	76.7/ 85.9
Average	63.6/62.5	87.8/71.0	85.6/81.0	89.1/84.7	79.9/ 87.4

Table 2: Anomaly detection and segmentation results with AUPRO/I-AUROC(%) on VisA.

	DRAEM[1]	PatchCore[13]	RD[2]	DiffusionAD[3]	Our-fp
Average	73.1/88.7	91.2/95.1	70.9/96.0	93.2/97.8	90.4/96.1

3 Experiments and Analysis

3.1 Experimental Settings

Datasets. **MVTec AD** and **VisA** feature high-resolution images across multiple object and texture categories, highlighting both surface and structural defects. **AeBAD-S** is specifically focused on domain diversity within aero-engine blade images. **GoodsAD** captures extensive intra-class diversity with 6,124 high-resolution images of common supermarket goods, showcasing a single product offered by multiple brands. **MAD** features images of LEGO animal toys, specifically designed to evaluate pose-agnostic tasks. Detailed information is presented in Appendix B.

Implementation. We utilized the pre-trained UniRepLKNet-N [22] on ImageNet [20] as the encoder. Network optimization was carried out using an AdamW optimizer [23], with the β parameters set to (0.9, 0.999) and a weight decay of 0.00005. The learning rate was set at 0.005, accompanied by an ExponentialLR scheduler with a gamma of 0.995. The batch size for all experiments was 16. The network was trained for varying epochs across different datasets: 240 epochs for GoodsAD, 150 epochs for MAD and ViSA, 130 epochs for AeBAD-S, and 160 epochs for the unified multiclass settings of MVTEC AD and ViSA. Results were reported from the **last epoch** for each scenario. Frames Per Second (FPS) tests were conducted on an NVIDIA GTX 1080Ti GPU with a batch size of 1, specifically omitting the efficient large-kernel convolution suggested by [20]. All other experiments, except for the FPS experiment, were performed on an NVIDIA RTX 4090 GPU using PyTorch 2.0.

Metrics. Image-level anomaly detection performance is quantified using the Area Under the Receiver Operator Curve (I-AUROC). For anomaly localization, we utilize two metrics: Area Under the Per-Region Overlap (AUPRO) and Area Under the Precision-Recall Curve (P-AUPR) [24]. AUPRO is designed to treat anomalous regions of various sizes equally, thus providing uniform sensitivity across different anomaly scales. P-AUPR is especially sensitive to datasets with imbalanced categories.

3.2 Anomaly Detection and Segmentation on FPADs

Anomaly detection and segmentation results on the AeBAD-S and VisA datasets are summarized in Tables 1 and 2, respectively. For the AeBAD-S dataset, our method achieved an I-AUROC of 87.4%, which surpasses the RD baseline by 6.4% and the previous state-of-the-art (SOTA) of 84.7% by 2.7%. However, there is a decrease in segmentation performance, with AUPRO 5.7% lower compared to RD. The reason for this situation may be that in images with more severe misalignment, the compacted data from our model may spread more significantly to the surrounding normal regions when a small anomaly is detected, thereby marking more normal regions as anomalous. Despite labeling additional areas as anomalous, the model effectively detects subtle anomalies. Additionally, for the VisA dataset, there is almost no improvement in the classification performance of our method; however, there is a notable improvement in segmentation, where the AUPRO score reached 90.4%, marking a substantial 19.5% increase over RD. This demonstrates that as long as the dataset does not exhibit extreme misalignment, our method achieves excellent segmentation performance.

Table 3: Anomaly detection result under unified setting with I-AUROC(%) on MVTec AD / VisA.

MVTec AD	/ VisA	RD[2]	UniAD[10]	ReContra[5]	Our-fr
Carpet	/ Candle	98.3/93.6	99.8/94.6	98.3/96.3	99.9/ 98.9
Grid	/ Capsules	99.0 /67.8	98.2/74.3	98.9/77.7	98.2/ 91.2
Leather	/ Cashew	100 /94.6	100 /92.6	100 /94.5	100 / 97.6
Tile	/ Chewinggum	98.1/95.3	99.3/98.7	99.5/98.6	100 / 99.0
Wood	/ Fryum	99.3/94.4	98.6/90.2	99.7 / 97.3	99.4/96.6
Bottle	/ Macaronil	79.9/97.2	99.7/91.5	100 /97.6	100 / 98.6
Cable	/ Macaroni2	86.8/86.2	95.2/83.6	95.6 / 89.5	99.0 /88.9
Capsule	/ PCB1	96.3/96.5	86.9/94.3	97.3 /96.5	96.0/ 98.0
Hazelnut	/ PCB2	100 /93.0	99.8/92.5	100 /96.8	100 / 97.0
MetalNut	/ PCB3	99.8/94.5	99.2/89.8	100 / 96.8	100 /97.8
Pill	/ PCB4	92.8/ 100	93.7/99.3	96.3/99.9	97.9 /99.8
Screw	/ Pipe fryum	96.5/99.7	87.5/97.3	97.2 /99.3	94.1/ 99.7
Toothbrust	/ -	97.5/-	94.2/-	96.7/-	98.9 /-
Transistor	/ -	93.3/-	99.8 /-	94.5/-	97.6/-
Zipper	/ -	98.6/-	95.8/-	99.4/-	99.7 /-
Average	/ Average	95.8/92.7	96.5/91.5	98.2/95.1	98.8 / 96.9

Table 4: Anomaly detection results with I-AUROC(%) on GoodsAD.

	RD [14]	SimpleNet [25]	ReContra [5]	PCore _{1%} [13]	PCore _{100%} [13]	Our-fr
cigarette box	65.1	97.8	86.2	98.8	99.2	98.1
drink bottle	67.2	70.0	69.6	77.2	81.4	80.4
drink can	63.3	70.8	73.8	86.3	93.9	90.3
food bottle	76.6	78.1	83.3	86.3	90.0	91.8
food box	63.3	72.0	65.5	72.7	74.3	77.8
food package	63.5	63.2	65.6	66.9	74.2	77.9
Average	66.5	75.3	74.0	81.4	85.5	86.1

Table 5: Anomaly segmentation results with P-AUPR/AUPRO(%) on GoodsAD.

	RD[14]	SimpleNet[25]	PCore _{1%} [13]	PCore _{100%} [13]	Our-fr
Average	15.4/79.7	24.4/68.8	51.6/80.5	53.8 / 89.9	46.0/87.5

3.3 Anomaly Detection and Segmentation on FRADs

We evaluated our MiniMaxAD-fr model under the unified setting on MVTec AD and VisA, hereafter referred to as Uni MVTec AD and Uni ViSA, respectively. The image-level anomaly detection results for both Uni ViSA and Uni MVTec AD are presented in Table 5. Our method achieves state-of-the-art (SOTA) performance on both datasets. Specifically, in Uni ViSA, MiniMaxAD-fr attains an I-AUROC of 96.9%, surpassing the previous SOTA of 95.1% held by ReContrast by a significant margin of 1.8%. Note that the I-AUROC of MiniMaxAD-fr in Uni ViSA increases by 0.5% compared to the one-category-one-model setting on ViSA; this supports our argument regarding the difficulty of converging to the global optimum for \mathcal{L}_{global} . It also suggests the potential for **unifying** FRADs and FPADs. We propose introducing irrelevant categories into FPADs to transform them into FRADs, using this strategy as a **strong regularization** that can promote **tighter embedding**, and optimizing them with \mathcal{L}_{adc} .

On the GoodsAD dataset, our method achieves an I-AUROC of 86.1%, marginally surpassing the previous SOTA held by PatchCore-100% by 0.6% and significantly outpacing it in inference speed at 40.7 FPS on a 1080ti GPU, which is 37 times faster. Moreover, it shows a substantial improvement of 19.6% over the baseline RD method. Additionally, for anomaly segmentation, it achieves an AUPRO of 87.5%, notably higher than the 80.5% achieved by PatchCore-1%, as detailed in Tables 3 and 4.

Table 6: Anomaly detection results with I-AUROC(%) on MAD-Sim.

	UniAD [10]	CFlow [4]	RD [2]	PCore _{100%} [13]	OmniposeAD [12]	Our-fr
Average	62.2	71.3	66.8	81.3	90.9	84.4

Table 7: Ablation study on five benchmarks, measured in I-AUROC(%).

		FRADs			FPADs	
		GoodsAD	Uni ViSA	Uni A-S&MVAD	AeBAD-S	ViSA
RD	RD + \mathcal{L}_{global}	66.5	92.7	76.2&89.6	81.0	96.0
	Our + \mathcal{L}_{local}	80.1	93.0	84.3&97.1	85.1	93.8
	Our + $\mathcal{L}_{local-hm}$	80.6	96.3	86.2&98.2	85.4	96.0
Our-fp	Our + \mathcal{L}_{global}	77.5	93.1	84.9&96.3	87.4	96.1
Our-fr	Our + \mathcal{L}_{adc}	86.1	96.9	87.2&98.4	83.9	95.6

In addition, we validate the significant potential of MiniMaxAD-fr for FRADs using the MAD-Sim dataset. Anomaly detection results, averaged across 20 categories, are presented in Table 6. Although our method does not outperform the NeRF-based [26] method OmniposeAD [12], it achieves an I-AUROC that is 3.1% higher than the non-NeRF-based SOTA method, PatchCore-100%. These extensive experiments clearly demonstrate MiniMaxAD-fr’s advantages in handling FRADs.

3.4 Ablation Study

A comprehensive ablation study is detailed in Table 7, validating the effectiveness of the proposed elements. Compared to RD, MiniMaxAD+ \mathcal{L}_{global} demonstrates a significant improvement in performance on FRADs and FPADs, affirming the suitability of large kernel convolutional networks with GRN units for the multi-scale reconstruction framework. Our asymptotic adaptive contraction strategy, which is tailored for FRADs based on \mathcal{L}_{local} , achieves optimal performance on FRADs. In contrast, the performance of MiniMaxAD+ \mathcal{L}_{adc} is degraded compared to MiniMaxAD+ \mathcal{L}_{global} on FPADs. This degradation occurs because \mathcal{L}_{adc} , although based on \mathcal{L}_{local} and advantageous in some aspects, disrupts global consistency. Specifically, fitting well in one region might lead to underfitting in other regions. However, transforming FPADs into FRADs is straightforward. As reported in the third column of our table, we merged scenarios to unify AeBAD-S with MVTec AD for training. Here we resize MVTec AD to 224×224 , other settings follow the default AeBAD-S. The results indicate that, with \mathcal{L}_{adc} , the model avoids focusing exclusively on one region and instead maintains global consistency using this strong regularization strategy. Further ablation studies, experimental results (including error bars), and qualitative visualizations are presented in the Appendix D.

4 Conclusion

In this study, we revisit existing UAD datasets, categorizing them into Feature-Rich Anomaly Detection Datasets (FRADs) and Feature-Poor Anomaly Detection Datasets (FPADs). For both datasets, we propose a unified solution that involves converting FPADs to FRADs. This approach significantly benefits our methodology, as the advantages clearly outweigh the disadvantages. To address the substantial intra-class diversity found in FRADs, we introduce MiniMaxAD, a novel multi-scale feature reconstruction paradigm that can efficiently model a large amount of information using smaller models, effectively addressing the limitations of low network capacity utilization prevalent in previous autoencoder-like UAD methods. Extensive testing on a range of established and challenging UAD datasets confirms the superiority of our approach. Our methodology holds significant potential to advance the development of methods based on multi-scale reconstruction.

Limitation. In this work, we avoided incorporating additional optimizations, such as the simulation of anomalies or the migration of pre-trained encoders from specific domains, in order to maintain efficiency and scalability. Additionally, MiniMaxAD’s smaller boost in processing FPADs compared to RDs may be a limitation, but in our methodology, converting FPADs to FRADs using the unified setting is a superior option, which improves performance while significantly reducing storage.

References

- [1] Vitjan Zavrtanik, Matej Kristan, and Danijel Skocaj. Dræm - A discriminatively trained reconstruction embedding for surface anomaly detection. In *2021 IEEE/CVF International Conference on Computer Vision, ICCV 2021, Montreal, QC, Canada, October 10-17, 2021*, pages 8310–8319. IEEE, 2021.
- [2] Tran Dinh Tien, Anh Tuan Nguyen, Nguyen Hoang Tran, Ta Duc Huy, Soan T.M. Duong, Chanh D. Tr. Nguyen, and Steven Q. H. Truong. Revisiting reverse distillation for anomaly detection. In *2023 IEEE/CVF Conference on Computer Vision and Pattern Recognition (CVPR)*, pages 24511–24520, 2023.
- [3] Hui Zhang, Zheng Wang, Zuxuan Wu, and Yu-Gang Jiang. Diffusionad: Denoising diffusion for anomaly detection, 2023.
- [4] Denis Gudovskiy, Shun Ishizaka, and Kazuki Kozuka. Cflow-ad: Real-time unsupervised anomaly detection with localization via conditional normalizing flows. In *2022 IEEE/CVF Winter Conference on Applications of Computer Vision (WACV)*, pages 1819–1828, Waikoloa, HI, USA, 2022. IEEE.
- [5] Jia Guo, shuai lu, Lize Jia, Weihang Zhang, and Huiqi Li. Reconcontrast: Domain-specific anomaly detection via contrastive reconstruction. In A. Oh, T. Neumann, A. Globerson, K. Saenko, M. Hardt, and S. Levine, editors, *Advances in Neural Information Processing Systems*, volume 36, pages 10721–10740. Curran Associates, Inc., 2023.
- [6] Kilian Batzner, Lars Heckler, and Rebecca König. Efficientad: Accurate visual anomaly detection at millisecond-level latencies, 2023.
- [7] Paul Bergmann, Michael Fauser, David Sattlegger, and Carsten Steger. Mvtec AD - A comprehensive real-world dataset for unsupervised anomaly detection. In *IEEE Conference on Computer Vision and Pattern Recognition, CVPR 2019, Long Beach, CA, USA, June 16-20, 2019*, pages 9592–9600. Computer Vision Foundation / IEEE, 2019.
- [8] Yang Zou, Jongheon Jeong, Latha Pemula, Dongqing Zhang, and Onkar Dabeer. Spot-the-difference self-supervised pre-training for anomaly detection and segmentation, 2022.
- [9] Paul Bergmann, Kilian Batzner, Michael Fauser, David Sattlegger, and Carsten Steger. Beyond dents and scratches: Logical constraints in unsupervised anomaly detection and localization. *International Journal of Computer Vision*, 130(4):947–969, 2022.
- [10] Zhiyuan You, Lei Cui, Yujun Shen, Kai Yang, Xin Lu, Yu Zheng, and Xinyi Le. A unified model for multi-class anomaly detection, 2022.
- [11] Jian Zhang, Runwei Ding, Miaoju Ban, and Linhui Dai. Pku-goodsad: A supermarket goods dataset for unsupervised anomaly detection and segmentation. *IEEE Robotics and Automation Letters*, 9(3):2008–2015, 2024.
- [12] Qiang Zhou, Weize Li, Lihan Jiang, Guoliang Wang, Guyue Zhou, Shanghang Zhang, and Hao Zhao. Pad: A dataset and benchmark for pose-agnostic anomaly detection, 2023.
- [13] Karsten Roth, Latha Pemula, Joaquin Zepeda, Bernhard Schölkopf, Thomas Brox, and Peter Gehler. Towards total recall in industrial anomaly detection, 2021.
- [14] Hanqiu Deng and Xingyu Li. Anomaly detection via reverse distillation from one-class embedding. In *IEEE/CVF Conference on Computer Vision and Pattern Recognition, CVPR 2022, New Orleans, LA, USA, June 18-24, 2022*, pages 9727–9736. IEEE, 2022.
- [15] Zilong Zhang, Zhibin Zhao, Xingwu Zhang, Chuang Sun, and Xuefeng Chen. Industrial anomaly detection with domain shift: A real-world dataset and masked multi-scale reconstruction. *Computers in Industry*, 151(C), 2023.
- [16] Mohammadreza Salehi, Niousha Sadjadi, Soroosh Baselizadeh, Mohammad H. Rohban, and Hamid R. Rabiee. Multiresolution knowledge distillation for anomaly detection. In *IEEE Conference on Computer Vision and Pattern Recognition, CVPR 2021, virtual, June 19-25, 2021*, pages 14902–14912. Computer Vision Foundation / IEEE, 2021.
- [17] Guodong Wang, Shumin Han, Errui Ding, and Di Huang. Student-teacher feature pyramid matching for anomaly detection, 2021.
- [18] Sergey Zagoruyko and Nikos Komodakis. Wide residual networks. In Richard C. Wilson, Edwin R. Hancock, and William A. P. Smith, editors, *Proceedings of the British Machine Vision Conference 2016, BMVC 2016, York, UK, September 19-22, 2016*. BMVA Press, 2016.

- [19] Sanghyun Woo, Shoubhik Debnath, Ronghang Hu, Xinlei Chen, Zhuang Liu, In So Kweon, and Saining Xie. Convnext v2: Co-designing and scaling convnets with masked autoencoders. In *Proceedings of the IEEE/CVF Conference on Computer Vision and Pattern Recognition*, pages 16133–16142, 2023.
- [20] Xiaohan Ding, Yiyuan Zhang, Yixiao Ge, Sijie Zhao, Lin Song, Xiangyu Yue, and Ying Shan. Unireplknet: A universal perception large-kernel convnet for audio, video, point cloud, time-series and image recognition, 2023.
- [21] Xiaohan Ding, Xiangyu Zhang, Ningning Ma, Jungong Han, Guiguang Ding, and Jian Sun. Repvgg: Making vgg-style convnets great again. In *IEEE Conference on Computer Vision and Pattern Recognition, CVPR 2021, virtual, June 19-25, 2021*, pages 13733–13742. Computer Vision Foundation / IEEE, 2021.
- [22] Jia Deng, Wei Dong, Richard Socher, Li-Jia Li, Kai Li, and Fei-Fei Li. Imagenet: A large-scale hierarchical image database. In *2009 IEEE Computer Society Conference on Computer Vision and Pattern Recognition (CVPR 2009), 20-25 June 2009, Miami, Florida, USA*, pages 248–255. IEEE Computer Society, 2009.
- [23] Ilya Loshchilov and Frank Hutter. Decoupled weight decay regularization. In *7th International Conference on Learning Representations, ICLR 2019, New Orleans, LA, USA, May 6-9, 2019*. OpenReview.net, 2019.
- [24] Paul Bergmann, Michael Fauser, David Sattlegger, and Carsten Steger. Uninformed students: Student-teacher anomaly detection with discriminative latent embeddings. In *2020 IEEE/CVF Conference on Computer Vision and Pattern Recognition, CVPR 2020, Seattle, WA, USA, June 13-19, 2020*, pages 4182–4191. IEEE, 2020.
- [25] Zhikang Liu, Yiming Zhou, Yuansheng Xu, and Zilei Wang. Simplenet: A simple network for image anomaly detection and localization, 2023.
- [26] Ben Mildenhall, Pratul P. Srinivasan, Matthew Tancik, Jonathan T. Barron, Ravi Ramamoorthi, and Ren Ng. Nerf: Representing scenes as neural radiance fields for view synthesis, 2020.
- [27] Christoph Baur, Benedikt Wiestler, Shadi Albarqouni, and Nassir Navab. Deep autoencoding models for unsupervised anomaly segmentation in brain mr images. In Alessandro Crimi, Spyridon Bakas, Hugo Kuijff, Farahani Keyvan, Mauricio Reyes, and Theo van Walsum, editors, *Brainlesion: Glioma, Multiple Sclerosis, Stroke and Traumatic Brain Injuries*, pages 161–169, Cham, 2019. Springer International Publishing.
- [28] Diederik P. Kingma and Max Welling. Auto-encoding variational bayes. In Yoshua Bengio and Yann LeCun, editors, *2nd International Conference on Learning Representations, ICLR 2014, Banff, AB, Canada, April 14-16, 2014, Conference Track Proceedings*, 2014.
- [29] Paul Bergmann, Sindy Löwe, Michael Fauser, David Sattlegger, and Carsten Steger. Improving unsupervised defect segmentation by applying structural similarity to autoencoders. In *Proceedings of the 14th International Joint Conference on Computer Vision, Imaging and Computer Graphics Theory and Applications*, pages 372–380, 2019.
- [30] Dong Gong, Lingqiao Liu, Vuong Le, Budhaditya Saha, Moussa Reda Mansour, Svetha Venkatesh, and Anton van den Hengel. Memorizing normality to detect anomaly: Memory-augmented deep autoencoder for unsupervised anomaly detection. In *2019 IEEE/CVF International Conference on Computer Vision, ICCV 2019, Seoul, Korea (South), October 27 - November 2, 2019*, pages 1705–1714. IEEE, 2019.
- [31] WenQian Liu, Runze Li, Meng Zheng, Srikrishna Karanam, Ziyang Wu, Bir Bhanu, Richard J. Radke, and Octavia I. Camps. Towards visually explaining variational autoencoders. In *2020 IEEE/CVF Conference on Computer Vision and Pattern Recognition, CVPR 2020, Seattle, WA, USA, June 13-19, 2020*, pages 8639–8648. IEEE, 2020.
- [32] Hyunjong Park, Jongyoun Noh, and Bumsu Ham. Learning memory-guided normality for anomaly detection. In *2020 IEEE/CVF Conference on Computer Vision and Pattern Recognition, CVPR 2020, Seattle, WA, USA, June 13-19, 2020*, pages 14360–14369. IEEE, 2020.
- [33] Ian J. Goodfellow, Jean Pouget-Abadie, Mehdi Mirza, Bing Xu, David Warde-Farley, Sherjil Ozair, Aaron C. Courville, and Yoshua Bengio. Generative adversarial nets. In Zoubin Ghahramani, Max Welling, Corinna Cortes, Neil D. Lawrence, and Kilian Q. Weinberger, editors, *Advances in Neural Information Processing Systems 27: Annual Conference on Neural Information Processing Systems 2014, December 8-13 2014, Montreal, Quebec, Canada*, pages 2672–2680, 2014.
- [34] Samet Akcay, Amir Atapour-Abarghouei, and Toby P. Breckon. Ganomaly: Semi-supervised anomaly detection via adversarial training, 2018.

- [35] Samet Akçay, Amir Atapour-Abarghouei, and Toby P. Breckon. Skip-ganomaly: Skip connected and adversarially trained encoder-decoder anomaly detection. In *2019 International Joint Conference on Neural Networks (IJCNN)*, pages 1–8, 2019.
- [36] Pramuditha Perera, Ramesh Nallapati, and Bing Xiang. OCGAN: one-class novelty detection using gans with constrained latent representations. In *IEEE Conference on Computer Vision and Pattern Recognition, CVPR 2019, Long Beach, CA, USA, June 16-20, 2019*, pages 2898–2906. Computer Vision Foundation / IEEE, 2019.
- [37] Thomas Schlegl, Philipp Seeböck, Sebastian M. Waldstein, Ursula Schmidt-Erfurth, and Georg Langs. Unsupervised anomaly detection with generative adversarial networks to guide marker discovery, 2017.
- [38] Thomas Schlegl, Philipp Seeböck, Sebastian M. Waldstein, Georg Langs, and Ursula Schmidt-Erfurth. F-anogan: Fast unsupervised anomaly detection with generative adversarial networks. *Medical Image Analysis*, 54:30–44, 2019.
- [39] Yufei Liang, Jiangning Zhang, Shiwei Zhao, Runze Wu, Yong Liu, and Shuwen Pan. Omni-frequency channel-selection representations for unsupervised anomaly detection. *IEEE Transactions on Image Processing*, 32:4327–4340, 2023.
- [40] Zhihao Gu, Liang Liu, Xu Chen, Ran Yi, Jiangning Zhang, Yabiao Wang, Chengjie Wang, Annan Shu, Guannan Jiang, and Lizhuang Ma. Remembering normality: Memory-guided knowledge distillation for unsupervised anomaly detection. In *2023 IEEE/CVF International Conference on Computer Vision (ICCV)*, pages 16355–16363, Paris, France, 2023. IEEE.
- [41] Geoffrey Hinton, Oriol Vinyals, and Jeff Dean. Distilling the knowledge in a neural network, 2015.
- [42] Xuan Zhang, Shiyu Li, Xi Li, Ping Huang, Jiulong Shan, and Ting Chen. Destseg: Segmentation guided denoising student-teacher for anomaly detection. In *2023 IEEE/CVF Conference on Computer Vision and Pattern Recognition (CVPR)*, pages 3914–3923, 2023.
- [43] Minghui Yang, Jing Liu, Zhiwei Yang, and Zhaoyang Wu. Slsg: Industrial image anomaly detection by learning better feature embeddings and one-class classification, 2023.
- [44] Jouwon Song, Kyeongbo Kong, Ye-In Park, Seong-Gyun Kim, and Suk-Ju Kang. Anoseg: Anomaly segmentation network using self-supervised learning, 2021.
- [45] Chun-Liang Li, Kihyuk Sohn, Jinsung Yoon, and Tomas Pfister. Cutpaste: Self-supervised learning for anomaly detection and localization. In *IEEE Conference on Computer Vision and Pattern Recognition, CVPR 2021, virtual, June 19-25, 2021*, pages 9664–9674. Computer Vision Foundation / IEEE, 2021.
- [46] Minghui Yang, Peng Wu, and Hui Feng. Memseg: A semi-supervised method for image surface defect detection using differences and commonalities. *Engineering Applications of Artificial Intelligence*, 119:105835, 2023.
- [47] Niv Cohen and Yedid Hoshen. Sub-image anomaly detection with deep pyramid correspondences, 2020.
- [48] Tiago S. Nazare, Rodrigo F. de Mello, and Moacir A. Ponti. Are pre-trained cnns good feature extractors for anomaly detection in surveillance videos?, 2018.
- [49] Paolo Napoletano, Flavio Piccoli, and Raimondo Schettini. Anomaly detection in nanofibrous materials by cnn-based self-similarity. *Sensors*, 18(1):209, 2018.
- [50] Niv Cohen, Issar Tzachor, and Yedid Hoshen. Set features for fine-grained anomaly detection, 2023.

Appendices

A Related Work

Methods based on reconstruction. In unsupervised anomaly detection (UAD), methods based on image-level reconstruction train models to reconstruct normal images, leveraging the assumption that anomalies will result in poor reconstruction quality due to model unfamiliarity with normal images. Early Autoencoder-based methods [27; 28; 29; 30; 31; 32] faced challenges with reconstruction quality, as did initial Generative Adversarial Network (GAN)-based approaches [33; 34; 35; 36; 37; 38]. Recently, OCR-GAN [39] improved the performances by decoupling input images into various frequency components, employing multiple generators for enhanced reconstruction. On the feature level, the introduction of the teacher-student model [24; 40; 14], inspired by knowledge distillation [41], utilizes a pre-trained network as a 'teacher' to guide a 'student' model trained only on normal images. This approach targets feature reconstruction, and more recently, EfficientAD [6] has cleverly integrated autoencoders to refine the learning process. Furthermore, ReContrast [5] incorporates an additional non-frozen, pre-trained encoder within the Reverse Distillation (RD) framework [14]. This encoder employs cross-reconstruction via contrast learning to reduce the semantic gap between pre-trained features and those observed in the unsupervised anomaly detection (UAD) scenario.

Methods based on simulated anomalies. This approach, which simulates anomalies to provide supervisory signals, includes various innovative methods [2; 25; 42; 43; 44]. For instance, [45] utilizes a technique where a portion of an image is cut and randomly pasted elsewhere to create forged anomalies. Moreover, DRAEM [1] employs Perlin noise to construct anomalies and segments these during training to generalize the segmentation capability to actual anomalies. More recently, MemSeg [46] attempted to simulate anomalies within the foreground region of images. However, the segmentation of the foreground region proved to be unstable. Furthermore, SimpleNet [25] introduces gaussian noise into the feature space to simulate anomalies. The effectiveness of these methods hinges on the extent to which the pseudo anomalies resemble actual anomalies and on the placement of these fabricated anomalies. Generalizing these methods to new datasets remains challenging, and there is considerable scope for improvement.

Methods Based on K-Nearest Neighbor (KNN). KNN-based methods leverage feature matching for inference, as demonstrated in various studies [47; 48; 49; 50]. One prominent example, PatchCore [13], utilizes a large pre-trained network to extract normal features and applies a core-set down-sampling technique to mitigate storage and inference costs. This approach has exhibited strong performance across diverse industrial anomaly detection datasets. Despite these advantages, the inference speed of PatchCore remains slow, and the costs associated with inference rise incrementally as the training sample size increases, due to the expanding memory bank.

B Datasets

MVTec AD is a widely recognized industrial anomaly detection dataset, comprising over 5,000 high-resolution images across fifteen distinct object and texture categories. Each category includes a set of defect-free training images and a test set featuring a range of defects as well as defect-free images. In our experiments, all images were resized to a uniform resolution of 256×256 .

VisA is a challenging anomaly detection dataset with 10,821 images across 12 subsets, each representing a different class of objects. The anomalies in these images include surface defects like scratches, dents, discoloration, or cracks, and structural defects such as misaligned or missing parts. We applied the unsupervised default settings [8] to segregate the training and test sets. In our experiments, all images were resized to a uniform resolution of 256×256 .

AeBAD-S shifts focus from the diversity of defect categories, as seen in datasets like MVTEC AD and VisA, to the diversity of domains within the same category. AeBAD-S aims to enhance the automation of anomaly detection in aero-engine blades, crucial for their stable operation. This dataset features various scales of individual blade images, characterized by non-aligned samples and a domain shift between the normal sample distribution in the test set and that in the training set, primarily due to variations in illumination and viewing angles. We resized the images to 256×256 and then center-cropped them to 224×224 for our experiments.

Table A1: Performance on AeBAD-S over three runs (%).

	I-AUROC	AUPRO
Same	86.27 \pm 0.45	78.47 \pm 0.21
Background	89.03 \pm 0.41	79.43 \pm 0.42
Illumination	85.87 \pm 0.68	83.73 \pm 0.29
View	86.93 \pm 0.54	76.27 \pm 0.31
Average	87.03 \pm 0.29	79.42 \pm 0.29

Table A2: Performance on GoodsAD over three runs (%).

	I-AUROC	AUPRO	P-AUPR
cigarette box	97.77 \pm 0.34	85.77 \pm 0.38	59.70 \pm 1.13
drink bottle	80.40 \pm 0.33	86.80 \pm 0.08	49.83 \pm 0.90
drink can	89.80 \pm 0.41	87.00 \pm 0.49	49.13 \pm 0.50
food bottle	91.20 \pm 0.45	92.60 \pm 0.16	62.13 \pm 0.37
food box	78.67 \pm 0.96	84.03 \pm 0.05	20.07 \pm 0.45
food package	76.50 \pm 1.07	86.90 \pm 0.29	31.27 \pm 0.26
Average	85.71 \pm 0.23	87.2 \pm 0.16	45.18 \pm 0.34

GoodsAD includes 6,124 images across six categories of common supermarket goods, captured at a high resolution of 3000×3000 . Each image features a single item, typically centered, with anomalies occupying only a small fraction of the image pixels. In our experiments, all images were resized to a uniform resolution of 224×224 .

MAD is the first dataset designed to evaluate pose-agnostic anomaly detection tasks. It includes over 4,000 high-resolution multi-pose RGB images of complexly shaped LEGO animal toys for training, and more than 7,000 simulated and real-world captured RGB images for testing, which include pixel-accurate ground truth annotations for three types of anomalies. The dataset is divided into MAD-Sim and MAD-Real, representing modeled and real image sets, respectively. In our experiments, we resized the resolution of all images to 400×400 .

C More Implementation Details

The results for the comparison methods on AeBAD-S [15] are derived from the original paper, while those for VisA come from DiffusionAD [3]. For GoodsAD [11], we have included image-level detection results from ReContrast [5], which we trained for 2000 iterations in our runtime environment using the default settings. We present the results of the last iteration, which are only 1.2% lower than those from the best iteration, with other results drawn from the original paper. The results for Uni MVTEC AD and Uni ViSA are taken from ReContrast. In addition, we supplemented the MAD-Sim dataset results with those from RD (using the default configuration) and the ensemble version of PatchCore-100%. Due to the incompatibility of the 400×400 input size with RD and MiniMaxAD, we used nearest neighbor interpolation to ensure the output size of the decoder matched that of the encoder.

D Additional Results

D.1 Additional Experimental Results

The results in the main paper are reported with a single random seed following our baseline [14]. In Tables A1 and A2, we report the mean and standard deviation of three runs with three different random seeds (1, 11 and 111) [5]. In addition to the averaged segmentation performances in Table 5, we present the AUPRO and P-AUPR of each category in GoodsAD in Table A3. Similarly, we complement the average detection performance in Table 4 by providing the I-AUROC for each category in MAD-Sim in Table A6.

Table A3: P-AUPR/AUPRO(%) of 6 subset (categories) on GoodsAD.

	RD[14]	SimpleNet[25]	PCore _{1%} [13]	PCore _{100%} [13]	Our-fr
cigarette box	23.7/72.7	54.1/90.3	71.6/93.4	73.0/94.0	61.3/86.3
drink bottle	12.5/84.2	20.8/66.5	65.8/84.2	66.4/90.6	51.0/86.7
drink can	17.4/81.9	18.7/67.0	54.1/78.0	61.1/91.2	49.8/87.6
food bottle	25.4/84.3	40.5/75.0	63.9/87.3	66.2/93.5	62.6/92.8
food box	5.8 /75.9	7.1 /56.4	19.8/68.2	19.8/83.1	19.7/ 84.1
food package	7.7 /79.4	5.6 /57.8	34.4/71.9	36.0/86.7	31.4/ 87.2
Average	15.4/79.7	24.4/68.8	51.6/80.5	53.8/89.9	46.0/87.5

Table A4: Ablation on the values of p_{hard} and p_{lim} in \mathcal{L}_{adc} on GoodsAD (%).

p_{lim}	0.999			0.9995			9999		
p_{hard}	0.9995	0.9999	1	0.9995	0.9999	1	0.9995	0.9999	1
I-AUROC	85.5	85.9	85.9	86.1	86.1	85.8	85.7	85.4	85.3

D.2 Additional Ablation Study

As shown in Table A4, we performed an ablation study of p_{hard} and p_{lim} in \mathcal{L}_{adc} . Intuitively, p_{hard} controls the decay rate and p_{lim} represents the lower limit of decay. The results show that \mathcal{L}_{adc} has the most stable performance at $p_{lim} = 0.9995$, where its performance is less affected by changes in p_{hard} . In addition, our ablation experiments on $\mathcal{L}_{local-hm}$ in Table A5 show that fixed mining strategy yields unsatisfactory results.

D.3 Alignment Process in Entropy Perspective

A high variance indicate greater diversity and potential for capturing complex patterns or relationships. More directly, information entropy, which focuses on the entropic properties of probability distributions (i.e., the uncertainty associated with these distributions), provides a more direct measure of the data’s informational content. firstly, we calculate the occurrence c_i of each feature f_i in the flattened feature maps $\mathcal{F}(f_E^k / \|f_E^k\|)$ and $\mathcal{F}(f_D^k / \|f_D^k\|)$, with a total count of N , where $N = C^k \times H^k \times W^k$. The probability of each feature f_i is then computed as:

$$p(f_i) = \frac{c_i}{N}$$

Subsequently, the entropy of the feature map is given by:

$$H(\mathcal{F}) = - \sum_{i=1}^n p(f_i) \log_2(p(f_i) + \epsilon)$$

where ϵ represents a very small positive number, n is the total number of different pixel values in feature maps. We calculated the mean of the entropy of the three layers of feature maps. The results depicted in Figure A1 demonstrate that, with the aid of the GRN unit, MiniMaxAD consistently generates feature maps that are richer in informative content. In contrast, the RD approach exhibits a trend towards degradation.

D.4 Qualitative Results and Analyze

In Figure A2, we display anomaly maps for 28 samples from GoodsAD (left) and MAD-Sim (right), and in Figure A3, we present anomaly maps for 11 samples each from Uni MVTec AD and Uni ViSA. Additionally, we include results for these samples from ViSA under the one-category-one-model setting. To ensure that the visualization results effectively highlight the key qualities of the methods, we employed Min-Max normalization for all anomaly maps produced by the different methods.

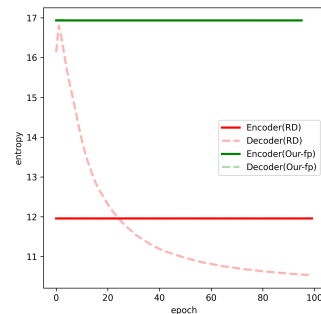


Figure A1: Feature alignment process of RD and MiniMaxAD when trained on *drink can*, viewed from the perspective of entropy, shows that the two green lines overlap.

Table A5: Ablation study on the values of p_{lim} in $\mathcal{L}_{local-hm}$ on GoodsAD (%).

p_{lim}	0.99	0.999	0.9995	0.9999
I-AUROC	77.9	81.5	80.6	77.3

Table A6: Performance of 20 subset (categories) of MAD-Sim (%).

	UniAD [10]	CFlow [4]	RD [2]	PCore _{100%} [13]	OmniposeAD [12]	Our-fr
Gorilla	56.6	69.2	75.5	71.0	93.6	71.5
Unicorn	73.0	82.3	73.9	91.8	94.0	93.7
Mallard	70.0	74.9	53.6	67.0	84.7	87.0
Turtle	50.2	51.0	77.0	87.2	95.6	85.8
Whale	75.5	57.0	59.2	86.5	82.5	80.1
Bird	74.7	75.6	74.5	80.3	92.4	90.3
Owl	65.3	76.5	70.2	78.4	88.2	82.6
Sabertooth	61.2	71.3	69.0	77.4	95.7	93.6
Swan	57.5	67.4	56.7	79.5	86.5	87.6
Sheep	70.4	80.9	76.9	90.1	90.1	96.2
pig	54.6	72.1	71.5	87.1	88.3	87.6
Zalika	50.5	66.9	57.6	78.2	88.2	79.5
Pheonix	55.4	64.4	58.6	68.6	82.3	75.1
Elephant	59.3	70.1	61.0	83.0	92.5	82.4
Parrot	53.4	67.9	51.9	78.0	97.0	77.8
Cat	53.1	65.8	65.4	84.9	84.9	70.8
Scorpion	69.5	79.5	67.4	86.6	91.5	87.0
Obesobeso	67.7	80.0	81.8	90.6	97.1	90.7
Bear	65.1	81.4	72.0	86.1	98.8	89.8
Puppy	55.6	71.4	62.3	72.7	93.5	77.9
Average	62.2	71.3	66.8	81.3	90.9	84.4

- **MiniMaxAD-fp** is equipped with \mathcal{L}_{global} . As evident from the anomaly maps of the GoodsAD samples, MiniMaxAD-fp handles the background more effectively than RD, which also uses \mathcal{L}_{global} . However, it still struggles to localize some of the more challenging anomalous regions.
- **MiniMaxAD-fr** is equipped with \mathcal{L}_{adc} and can accurately respond to difficult anomalous regions on FRADs, thanks to the adaptive contraction strategy. It tends to treat background and foreground more equally. For some of the more challenging images, it may exhibit large fluctuations in the background region, but it still significantly represents the anomalous regions, such as in the second row of GoodsAD and the penultimate six rows of MAD-Sim in Figure A2, and most of the images in Figure A3.
- **RD** appears less effective in coping with the FRADs, exhibiting more false alarms. Notably, RD shows some unexpected false alarms in Uni MVTec AD, particularly in the fourth vs. seventh columns of Figure A3. We hypothesize that this is due to the low effective capacity of RD, and that the extreme intraclass diversity of Uni MVTec AD contributes to an outlier bias in the model’s memorization of normal samples.
- **PatchCore** holds an advantage in dealing with FRADs. Its memory bank of normal features enables it to effectively detect regions that closely resemble the training set samples (e.g., backgrounds and identical poses). However, its feature query inference process is more vulnerable to domain shift, a phenomenon that is also subtly evident in the general dataset. This susceptibility increases the likelihood of generating false positives in cases of Domain Shift-specific challenges, as also supported by experiments on AeBAD-S, which specializes in domain shift.

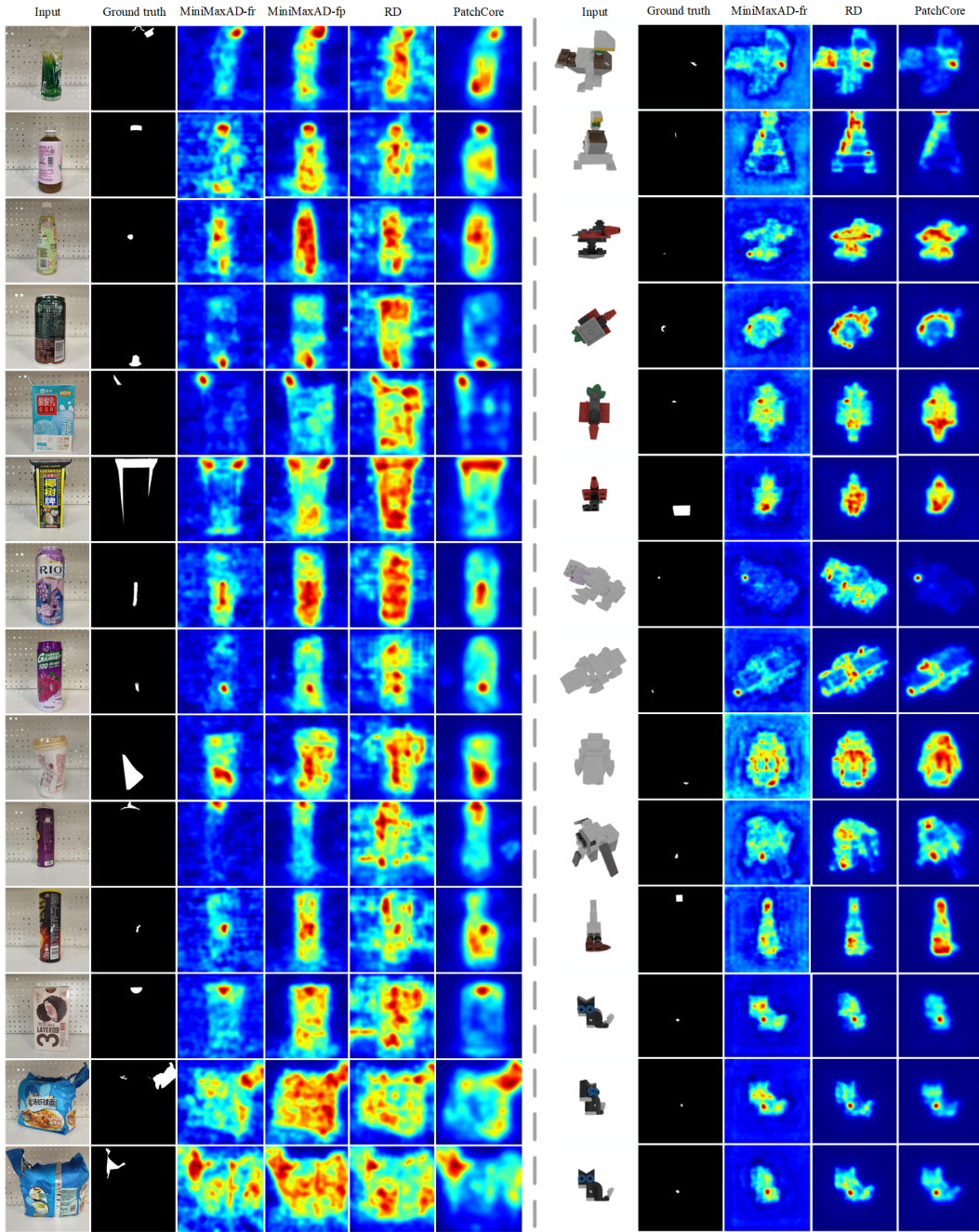


Figure A2: Anomaly maps on anomalous images from GoodsAD and MAD-Sim.

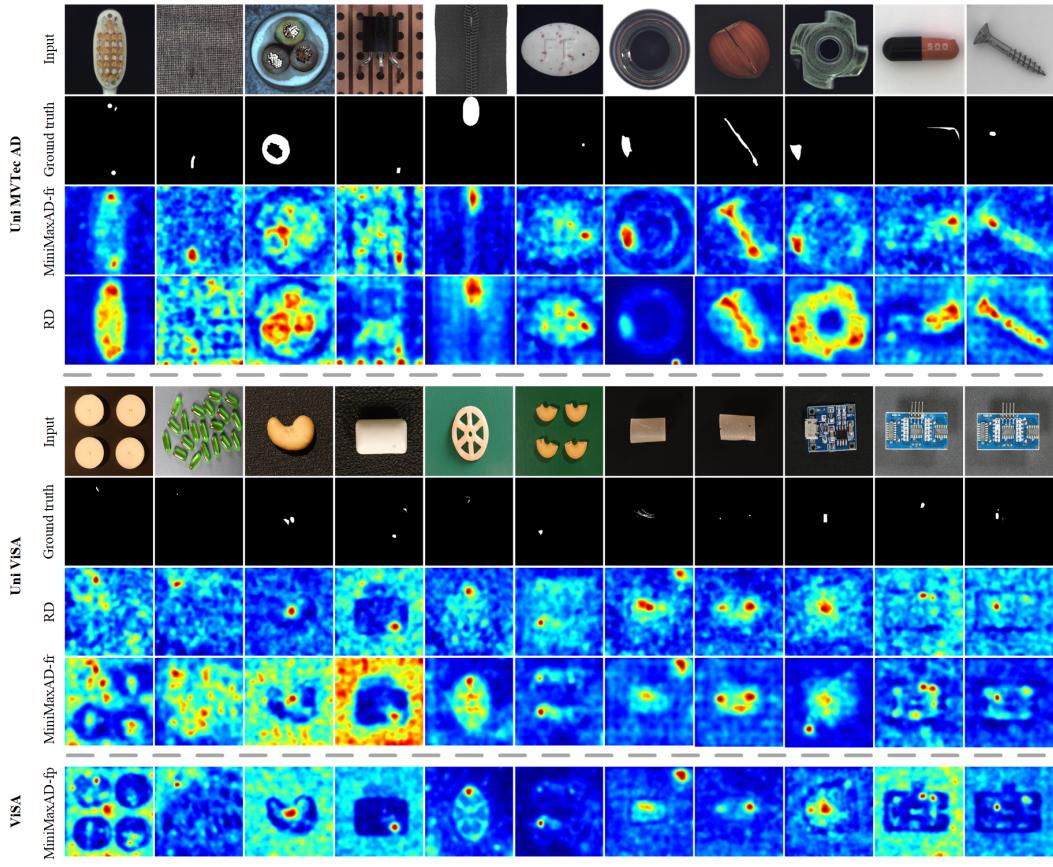


Figure A3: Anomaly maps on anomalous images from MVTec AD and ViSA. We show results for the unified setting as well as one-category-one-model setting.